processes

MDPI

*Article*

# Deformation-Control Performance of Pile Reinforcement for a Large Stilling Basin on a Heterogeneous Weak-Rock Foundation

**Liang Yin [1], Weiwei Wu [1], Ming Jiang [1], Wei Li [1], Kuanxing Zhu [2,3,*] and Qingxiang Meng [3]**

[1] PowerChina Huadong Engineering Corporation, Hangzhou 311122, China; yin_l@hdec.com (L.Y.); wu_ww@hdec.com (W.W.); jiang_m2@hdec.com (M.J.); li_w3@hdec.com (W.L.)
[2] State Key Laboratory of Hydraulic Engineering Intelligent Construction and Operation, Tianjin University, Tianjin 300072, China
[3] School of Earth Sciences and Engineering, Hohai University, Nanjing 210098, China; mqx@hhu.edu.cn
* Correspondence: 20250930@hhu.edu.cn

**Abstract**

Large stilling basins founded on heterogeneous weak-rock foundations may experience nonuniform deformation due to spatial variations in foundation stiffness. Although pile reinforcement is widely used for deformation control, its effectiveness may vary with local structure–foundation conditions. Overall and local deformation may also respond differently to pile parameters. This study conducted three-dimensional FLAC3D analyses of the Kala Hydropower Station stilling basin under the check-flood condition. Two representative transverse sections with different weak-rock distributions, pile embedment conditions, and structural configurations were compared under unreinforced and pile-reinforced conditions. The maximum resultant displacement ($U_{max}$) and maximum vertical joint offset ($\Delta U_{joint}$) were used to characterize overall and local differential deformation, respectively. Under the 2.5 m × 2.5 m pile layout, $U_{max}$ and $\Delta U_{joint}$ decreased by only 3.1% and 3.2% in Section 14–14, compared with 33.7% and 58.9% in Section 16–16. The two deformation measures also responded differently to pile spacing and pile length, and denser layouts or longer piles did not consistently reduce both overall and local deformation. Varying the thickness of competent rock overlying the weak rock produced only small changes in deformation, whereas increasing the weak-rock deformation modulus reduced both deformation measures, particularly in Section 16–16. These findings show that the effectiveness of pile reinforcement varies among structural locations with different foundation and embedment conditions. Pile layouts should therefore be evaluated for individual structural locations using both overall displacement and joint differential movement.

**Keywords:** heterogeneous weak-rock foundation; stilling basin; pile reinforcement; deformation control; spatially variable response; structural joints

Check for updates

Academic Editor: Qingbang Meng

Received: 27 August 2026
Revised: 30 September 2026
Accepted: 12 October 2026
Published: 26 October 2026

**Copyright:** © 2026 by the authors. Licensee MDPI, Basel, Switzerland. This article is an open access article distributed under the terms and conditions of the Creative Commons Attribution (CC BY) license.

## 1. Introduction

Large hydraulic structures are often founded directly on natural rock masses, whose spatial variability in lithology, integrity, and mechanical properties can strongly influence the response of the structure–foundation system [1–3]. Localized weak rock zones may further increase the nonuniformity of foundation deformation [4,5]. For large stilling basins with relatively continuous structural configurations, self-weight, water pressure, and uplift pressure act jointly on the structure–foundation system. Local changes in foundation stiffness may therefore lead to differential settlement between different parts of the structure, together with differential deformation and stress redistribution near

structural joints and stiffness-transition zones [6–9]. Because a stilling basin is divided into multiple structural blocks, relatively small changes in overall deformation may coexist with appreciable relative displacement across structural joints. Therefore, both overall structural deformation and relative displacement between adjacent blocks need to be considered when evaluating deformation performance.

In engineering practice, pile foundations are commonly used to improve deformation compatibility in structure–foundation systems. By modifying local support conditions, piles can restrain deformation in weak foundation zones and reduce differential movement between adjacent structural components [10,11]. Previous studies have shown that their deformation-control performance is affected by pile geometry, layout, and the relative stiffness between the piles and surrounding rock [12,13]. Chen et al. [12] systematically investigated the effects of rock-socketed length, pile spacing, pile-to-rock modulus ratio, slenderness ratio, and rock-mass stratification on the vertical response of rock-socketed pile groups. These factors were found to influence foundation settlement, load distribution among piles, and the overall pile-group response [12,14]. In particular, the reduction in pile-cap settlement became less pronounced as pile spacing increased [15,16]. Rock-socketed length should also be selected according to settlement-control requirements and local engineering conditions rather than increased indiscriminately [17]. These results indicate that the relationship between pile parameters and deformation-control performance is not necessarily monotonic [16,18]. In addition, different pile configurations may affect overall deformation and local relative deformation differently [19,20]. Therefore, a single overall displacement measure may not fully reflect the deformation-control performance of pile reinforcement.

The deformation-control performance of pile reinforcement is not determined solely by pile parameters. Local geological conditions and the spatial relationship between piles and weak geological units can also influence the structural response [21–23]. Previous studies have shown that rock-mass stratification, weak zones, and other local stiffness variations may lead to pronounced spatial differences in pile displacement, rotation, and internal forces [24–26]. This issue is particularly important for large continuous structures that extend across different rock-mass conditions [25–27]. Most existing studies have focused on pile response or deformation within a local foundation zone [14,28–30]. Few studies have systematically examined whether piles with the same prescribed spacing and length provide comparable deformation control at different locations of a continuous structure founded on heterogeneous rock. In addition, overall structural deformation and local joint offset are rarely examined together when assessing changes in pile spacing or pile length. It therefore remains unclear whether a pile configuration that reduces the maximum structural displacement also improves deformation compatibility across structural joints, and how much additional deformation control can be achieved by further increasing pile density or pile length after reinforcement. These questions are relevant to engineering design because different parts of the same hydraulic structure may overlie rock masses with different stiffnesses and weak rock distributions.

The stilling basin of the Kala Hydropower Station is founded on a markedly heterogeneous rock mass. Low-strength sericitized slate with a low deformation modulus occurs locally within the foundation and is spatially associated with rock masses of different engineering classes and structural discontinuities [31,32]. Previous studies on the Kala project examined the flood-discharge and energy-dissipation layout, the three-dimensional response of the stilling-basin–foundation system [31], and the stability of the left-bank slope [33]. These analyses incorporated the principal geological structures and identified nonuniform deformation near structural joints adjacent to the weak rock zone. However, the deformation-control effects of pile reinforcement at different parts of the stilling basin

have not been quantitatively compared, nor have the responses of overall deformation and local joint offset to changes in pile configuration been examined together. The influence of local foundation conditions on these differences also remains insufficiently quantified.

This study uses three-dimensional numerical analysis to evaluate the deformation-control performance of pile reinforcement for the Kala stilling basin. Two representative transverse sections, 14–14 and 16–16, are examined under unreinforced and pile-reinforced conditions. The two sections differ in weak-rock distribution and overlying structural components, allowing the performance of piles with the same spacing and length to be compared at different locations of the stilling basin. The maximum resultant displacement and the maximum vertical joint offset are used to characterize the overall deformation of the structure and the differential deformation between adjacent structural blocks, respectively. Pile spacing, pile length, the thickness of competent rock above the weak rock, and the weak rock deformation modulus are then varied to examine their effects on structural deformation. The results can support the selection and adjustment of pile arrangements according to structural location, local foundation conditions, and deformation control requirements.

## 2. Engineering Setting and Numerical Methodology

### *2.1. Study Area*

The Kala Hydropower Station is located on the main stem of the Yalong River in Muli Tibetan Autonomous County, Liangshan Yi Autonomous Prefecture, Sichuan Province, China. The dam site is situated in a deeply incised, V-shaped valley within a high-mountain gorge region, with a relative relief of approximately 600–700 m between the two banks. The location and topographic setting of the study area are shown in Figure 1.

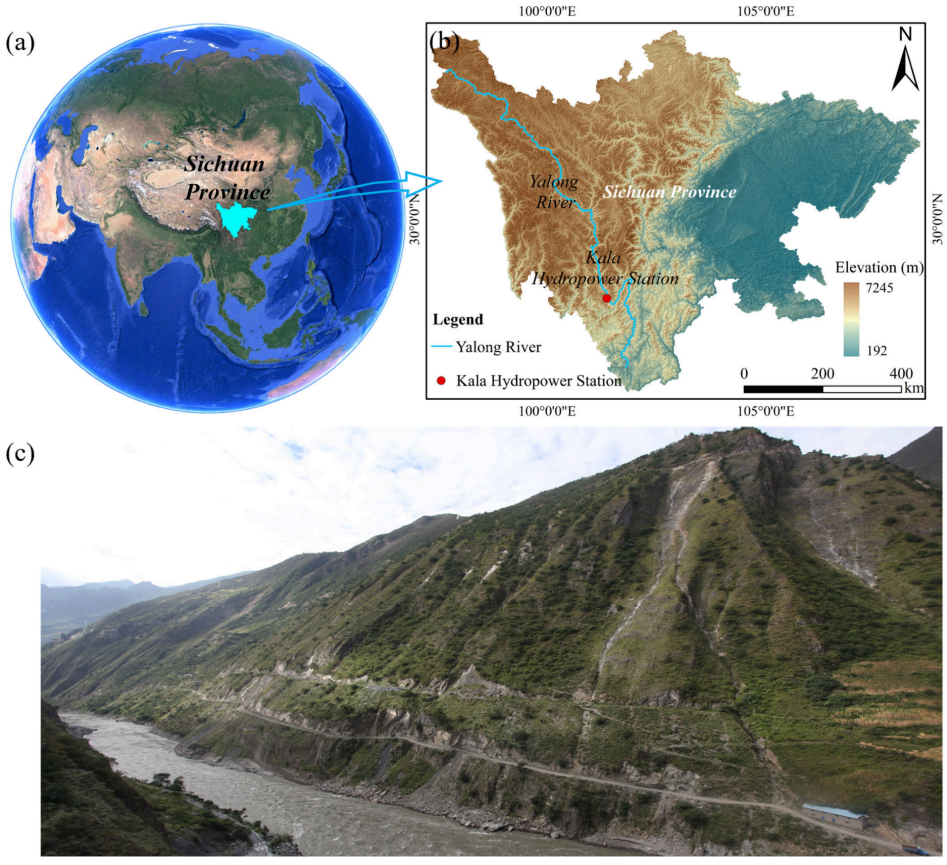


**Figure 1.** Geographical location and topographic setting of the study area. (**a**) Location of Sichuan Province in China; (**b**) location of the Kala Hydropower Station in Sichuan Province; (**c**) field photograph of the geomorphology of the project area.

The project includes a roller-compacted concrete gravity dam, flood-discharge structures, a downstream stilling basin, and a water-conveyance and power-generation system. The flood-discharge structures are arranged in the riverbed section, and an underflow stilling basin is used for energy dissipation downstream of the dam. The stilling basin investigated in this study is aligned with the flood-discharge centerline and extends from the dam toe to immediately upstream of the end sill. It is 96.13 m long and has a clear floor width of 71.0 m. The floor elevation ranges from 1882.0 to 1889.0 m. The stilling basin consists of reinforced concrete floor slabs, sidewalls, and an end sill, and is divided into structural blocks by five longitudinal and six transverse structural joints. The plan layout of the stilling basin is shown in Figure 2a.

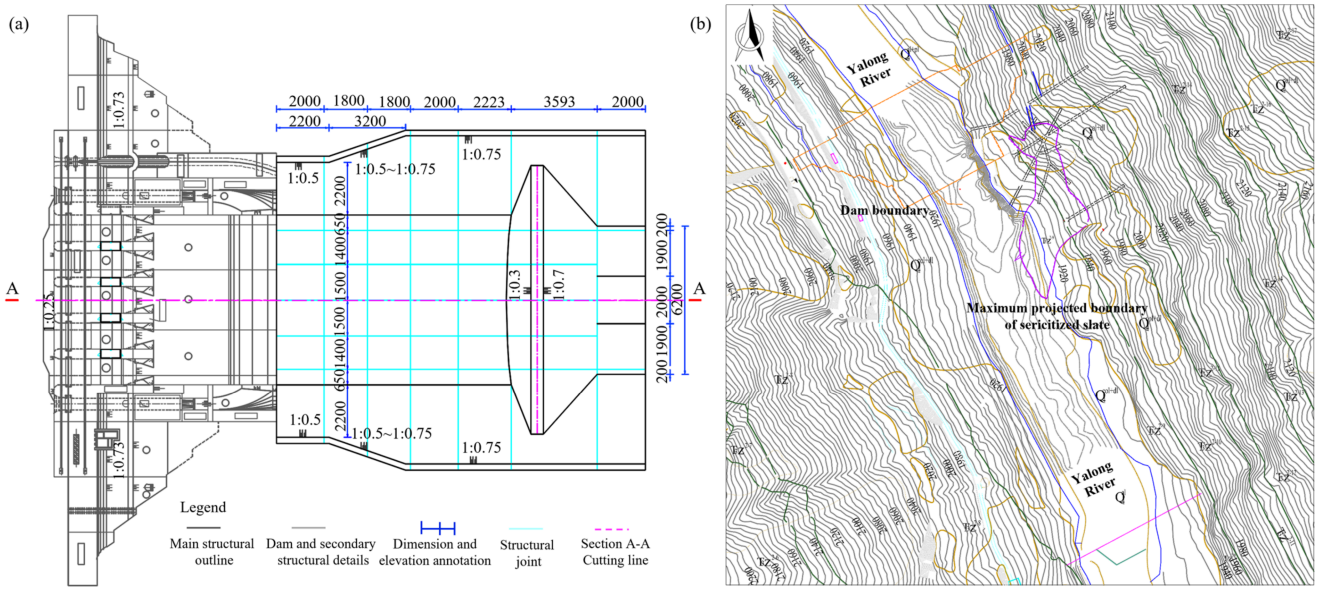


**Figure 2.** Structural layout and geological setting of the stilling basin. (**a**) Plan layout of the stilling basin; (**b**) projected distribution of sericitized slate.

### *2.2. Geotechnical Properties*

The bedrock in the dam-site area mainly comprises metamorphic sandstone, sandy slate, carbonaceous slate, and locally distributed marble of the Upper Triassic Zagunao Formation. Metamorphic sandstone and sandy slate are the dominant rock types beneath the stilling basin. The foundation is intersected by faults, interlayer compression zones, joints, and fractures. These geological structures, together with variations in lithology and rock-mass quality, produce marked spatial heterogeneity within the foundation.

Sericitized slate occurs locally beneath the left-bank part of the stilling basin and forms the principal weak-rock unit considered in this study. It has a broadly lens-shaped distribution, extending approximately 165 m in the upstream–downstream direction and 20–75 m in width. Its lateral extent and burial depth vary across the foundation, and it is locally interbedded with stronger surrounding rock masses. The projected distribution of the sericitized slate is shown in Figure 2b. The rock is weakly cemented, has low strength and stiffness, and is susceptible to softening and disintegration after wetting.

The physical and mechanical properties of the sericitized slate were determined from laboratory tests conducted during the design-stage engineering geological investigation. Representative cores were prepared as cylindrical specimens approximately 50 mm in diameter, with a height-to-diameter ratio of about 2.0. Both dry and saturated specimens were subjected to uniaxial compression tests. For saturation, the specimens were progressively immersed in water and then maintained under full immersion for 48 h. After the

surface water had been removed, the saturated specimens were tested immediately. The dry and saturated uniaxial compressive strengths ranged from 5.0 to 8.0 MPa and from 0.8 to 4.0 MPa, respectively. The softening coefficients calculated for paired sets of dry and saturated specimens ranged from 0.38 to 0.42.

The numerical model adopted engineering-scale rock mass parameters established from the engineering geological investigation, laboratory testing, rock mass classification, and design-stage evaluation. The parameters were adopted according to the moisture conditions under which they were determined. Saturated properties were used for parameters obtained under saturated conditions, whereas dry-state properties were retained where they were determined under dry conditions. No conversion between dry and saturated properties was introduced. For the sericitized slate, the deformation modulus and Poisson's ratio recommended for engineering-scale analysis ranged from 0.03 to 0.50 GPa and from 0.32 to 0.38, respectively. Based on the spatial variation identified in the geological investigation, the sericitized slate was represented by three layers in the numerical model. A deformation modulus of 0.055 GPa was assigned to Layer 1, whereas 0.035 GPa was assigned to Layers 2 and 3.

### *2.3. Structural Characteristics and Pile Reinforcement Scheme*

The floor slab, sidewalls, and end sill are cast-in-place reinforced-concrete structures. The floor slab is approximately 6 m thick. The sidewalls follow the excavated slopes and have a top thickness of approximately 2.5 m and a maximum base width of approximately 6.5 m. The locations of Sections 14–14 and 16–16 and their baseline pile layouts are shown in Figure 3.

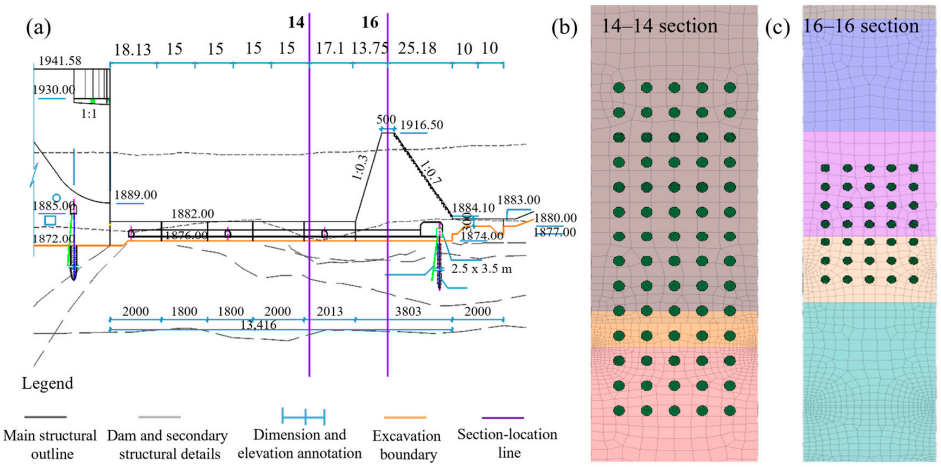


**Figure 3.** Representative sections and pile reinforcement layouts. (**a**) Locations of Sections 14–14 and 16–16; (**b**) baseline pile layout for Section 14–14; (**c**) baseline pile layout for Section 16–16.

Reinforcing piles were arranged beneath the parts of the stilling-basin floor affected by the weak rock. The piles had a circular cross-section with a diameter of 1.0 m and were represented by three-dimensional solid zones in the numerical model. The piles were assigned the material properties of C30 concrete, with a unit weight of 25 kN/m$^3$, an elastic modulus of 30.0 GPa, a Poisson's ratio of 0.167, a design tensile strength of 1.43 MPa, and a design compressive strength of 14.3 MPa.

The unreinforced foundation was used as the reference condition. The baseline cases for both representative sections used a transverse pile spacing of 2.5 m, a longitudinal pile spacing of 2.5 m, and a pile length of 30 m. The same pile material properties were used in both sectional models. Hereafter, pile spacing is expressed as transverse spacing × longitudinal spacing. Three plan layouts were examined: 2.5 m × 2.5 m,

2.5 m × 5.0 m, and 3.0 m × 3.0 m. The pile length was fixed at 30 m in the pile-spacing analysis. Within each section, the structural geometry, material properties, boundary conditions, and external loads were kept unchanged when the pile spacing was varied.

Two transverse sections, 14–14 and 16–16, were selected according to the structural zoning of the stilling basin and the spatial distribution of the weak rock. Section 14–14 represents the central part of the stilling basin above the main sericitized slate zone, where the weak rock has a relatively large lateral extent and variable burial depth. Section 16–16 passes through the end-sill axis and includes the end sill, adjacent structural blocks, and the underlying weak rock. Although the baseline cases had the same pile spacing and length, the piles passed through different distributions of sericitized slate and surrounding rock because the weak-rock geometry differed between the two sections. The piles in Section 14–14 were located beneath the central floor slab, whereas those in Section 16–16 were associated with the end sill and adjacent structural blocks. The two sections were therefore used to compare pile-reinforcement responses under different rock distributions and structural arrangements.

Pile spacing was examined in both sections with the pile length fixed at 30 m. Pile length was examined only in Section 14–14 because this section crosses the main sericitized slate zone and shows marked variation in weak-rock burial depth. For this analysis, the pile spacing was fixed at 3.0 m × 3.0 m, and pile lengths of 15, 20, 25, and 30 m were considered. This arrangement allowed the effects of pile spacing and pile length to be examined separately.

### *2.4. Numerical Model and Loading Condition*

A three-dimensional finite-difference model of the stilling basin and its rock foundation was developed using FLAC3D 9.0 (Itasca Consulting Group, Inc., Minneapolis, MN, USA). The model geometry was established from the project topography, structural drawings, and engineering geological data. An overall three-dimensional model was used to represent the spatial relationships among the topography, stilling-basin structure, and principal geological units. Separate three-dimensional sectional models were developed for Sections 14–14 and 16–16 to compare the effects of pile configurations and weak-rock conditions. The overall model, principal geological units, and sectional models are shown in Figure 4.

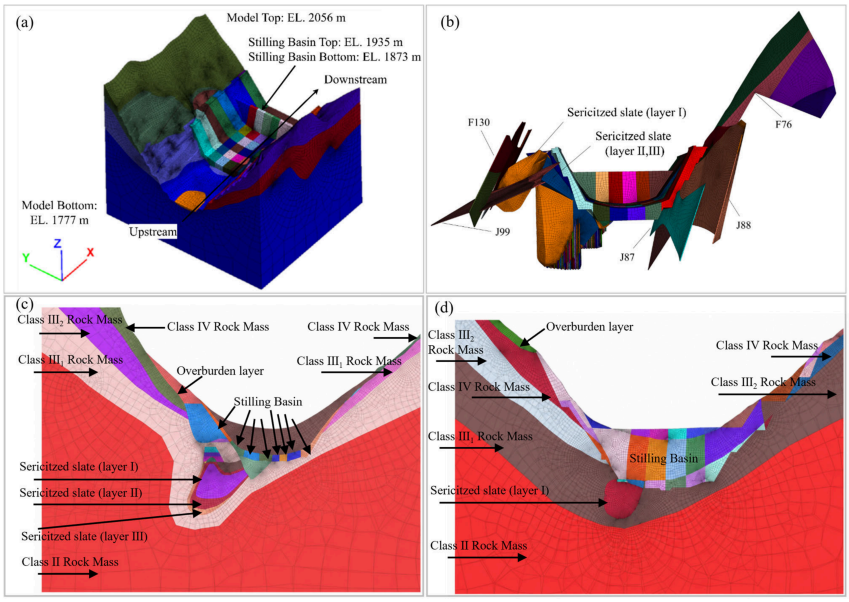


**Figure 4.** Numerical models used in the analysis. (**a**) Overall three-dimensional finite-difference model; (**b**) major geological units; (**c**) three-dimensional sectional model of the 14–14 section; (**d**) three-dimensional sectional model of the 16–16 section.

The overall model extended 150 m from the riverbed centerline toward each bank and 250 m in the upstream–downstream direction, with a bottom elevation of 1777 m. In the overall model, the $X$-axis was oriented downstream, the $Y$-axis was oriented transversely from the right bank toward the left bank, and the $Z$-axis was vertical and positive upward. The model included Class II, $III_1$, $III_2$, and IV rock masses, three layers of sericitized slate, and the principal geological structures J99, f130, J87, J88, and f76. The sectional models used a local coordinate system in which the $x$-axis was transverse to the river, the $y$-axis was oriented downstream, and the $z$-axis was vertical and positive upward. The Section 14–14 model was 500 m wide in the transverse direction, 15 m thick in the upstream–downstream direction, and approximately 453.1 m high. The corresponding dimensions of the Section 16–16 model were 360 m, 15 m, and approximately 310.3 m. Vertical displacement was constrained at the base of each model, while displacement normal to each boundary was constrained on the four vertical sides. The same boundary scheme was applied to the overall and sectional models.

The rock masses, sericitized slate, and principal geological structures were described using the Mohr–Coulomb elastoplastic model. Their elastic response was defined by the deformation modulus, $E$, and Poisson's ratio, $\nu$, while their shear strength was represented by the cohesion, c′, and internal friction angle, $\varphi$, where $f' = \tan\varphi$. Shear yielding occurred when the stress state of a rock zone reached the Mohr–Coulomb yield surface defined by c′ and $\varphi$. The local strength reserve of the foundation rock was evaluated using a point safety factor defined from the stress state of each rock zone relative to the Mohr–Coulomb yield surface. A value greater than 1.0 indicates that the stress state remains within the yield surface, whereas a value approaching 1.0 indicates that the rock zone is close to yielding. The material parameters were selected from the design-stage engineering geological investigation, laboratory and field tests, rock-mass classification, and engineering recommendations, as summarized in Table 1. The stilling-basin structure and reinforcing piles were represented by three-dimensional solid zones. The concrete components, including the piles, were modeled as linear-elastic materials. At the pile–rock boundaries, the pile and surrounding rock zones shared grid nodes. The pile–rock connection was therefore represented as fully bonded, and no separate interface elements with independent normal and shear stiffnesses or slip and separation criteria were introduced. This treatment was applied consistently to all pile-reinforced cases. The mesh was locally refined around the piles and at locations with pronounced changes in structural or geological geometry. Eight-node hexahedral zones were used wherever practicable, while four-node tetrahedral zones were introduced in geometrically complex transition regions. The overall model contained 5,841,633 zones and 2,550,615 grid points.

The structural joints, which were approximately 20 mm wide, were represented by interface elements between adjacent concrete blocks rather than explicitly discretized using solid zones. This treatment avoided excessively small solid zones. The same interface formulation and parameters were used in all comparative analyses. The structural-joint interfaces were treated independently from the fully bonded pile–rock boundaries. The interface elements permitted relative movement between adjacent concrete blocks, whereas load transfer between the piles and surrounding rock occurred through the shared grid nodes.

All comparisons of pile spacing, pile length, and weak-rock properties were conducted under the check-flood condition. Each model was first brought to equilibrium under self-weight, and the resulting stress state was used as the initial condition for the hydraulic loading stage. Within each parametric series, only the parameter under investigation was varied; the remaining geometry, material properties, boundary conditions, and loads were unchanged.

**Table 1.** Material parameters adopted in the numerical models.

| Material/Rock Mass | Unit Weight $\gamma$ (kN/m$^3$) | Elastic/Deformation Modulus E (GPa) | Poisson's Ratio $\nu$ | Friction Coefficient f′ | Cohesion c′ (MPa) |
|---|---|---|---|---|---|
| C30 concrete for piles | 25.0 | 30.0 | 0.167 | – | – |
| C25 concrete | 25.0 | 28.0 | 0.167 | – | – |
| C20 concrete | 24.0 | 25.5 | 0.167 | – | – |
| Sericitized slate, Layer 1 | 19.6 | 0.055 | 0.32 | 0.50 | 0.25 |
| Sericitized slate, Layers 2–3 | 19.4 | 0.035 | 0.38 | 0.45 | 0.15 |
| Class II rock mass | 27.6 | 21.5 | 0.19 | 1.45 | 1.76 |
| Class $III_1$ rock mass | 27.5 | 13.0 | 0.23 | 1.15 | 1.45 |
| Class $III_2$ rock mass | 27.4 | 5.0 | 0.25 | 1.05 | 1.10 |
| Class IV rock mass | 26.5 | 2.25 | 0.30 | 0.75 | 0.45 |
| J99 | 23.5 | 1.25 | 0.35 | 0.50 | 0.11 |
| f130 | 23.0 | 0.75 | 0.40 | 0.48 | 0.11 |
| J87 | 23.5 | 1.25 | 0.35 | 0.48 | 0.11 |
| J88 | 23.5 | 1.25 | 0.35 | 0.43 | 0.09 |
| f76 | 23.0 | 0.75 | 0.35 | 0.45 | 0.11 |

Note: The modeled widths of J99, f130, J87, J88, and f76 were 0.10, 0.20, 0.25, 0.25, and 0.50 m, respectively. A dash indicates that Mohr–Coulomb shear-strength parameters were not assigned to the linear-elastic concrete materials.

Under the check-flood condition, the downstream water level was 1934.24 m. Water pressure was applied to the submerged surfaces of the floor slab and sidewalls and consisted of mean and fluctuating components. The mean pressure was calculated from the water depth above each point, and no water pressure was applied to parts of the sidewalls above the downstream water level. Based on the hydraulic model tests, the standard deviation of the fluctuating pressure was 7.84 kPa. Three times this value was adopted as the representative fluctuating pressure. After applying an area-averaging coefficient of 0.55, the fluctuating pressure applied to the structural surfaces was 12.9 kPa. Uplift pressure was applied to the underside of the floor slab and sidewalls and was calculated from the hydraulic head difference between the downstream water level and the elevation of the point considered. A reduction coefficient of 0.4 and a partial load factor of 1.2 were applied. The same water and uplift pressures were used in all comparative cases.

### *2.5. Deformation Measures for Comparative Assessment*

The resultant displacement at each point in the model was calculated as:

$$U = \sqrt{U_x^2 + U_y^2 + U_z^2} \quad (1)$$

where $U_x$, $U_y$ and $U_z$ are the displacement components in the three coordinate directions. In the sectional models, these components represent transverse, upstream–downstream, and vertical displacement, respectively. The maximum value of $U$ within the concrete stilling-basin structure was defined as the maximum resultant displacement, $U_{max}$, and used to characterize the overall deformation magnitude. The distributions of $U_x$ and $U_z$ were also examined to identify the dominant displacement components and the locations of deformation concentration.

Local differential deformation was quantified using the maximum vertical joint offset, $\Delta U_{joint}$. At corresponding locations on the two sides of a structural joint, the vertical joint offset was calculated as the difference between the vertical displacements of the adjacent concrete blocks. The largest absolute difference among the examined joints was defined as:

$$\Delta U_{\text{joint}} = \max\left|U_z^{(+)} - U_z^{(-)}\right| \quad (2)$$

where $U_z^{(+)}$ and $U_z^{(-)}$ are the vertical displacements of the adjacent blocks on the two sides of the joint. Accordingly, $U_{max}$ represents the overall deformation magnitude of the stilling-basin structure, whereas $\Delta U_{joint}$ represents differential vertical movement between adjacent structural blocks.

The change in each deformation measure after pile reinforcement was expressed by the relative reduction ratio, $R_D$:

$$R_D = \frac{D_0 - D_p}{D_0} \times 100\% \quad (3)$$

where $D_0$ and $D_p$ are the values of $U_{max}$ or $\Delta U_{joint}$ under the unreinforced and pile-reinforced conditions, respectively. A positive $R_D$ indicates a decrease in the corresponding deformation measure after reinforcement, whereas a negative value indicates an increase. The deformation-control performance was evaluated from $U_{max}$, $\Delta U_{joint}$, and the spatial distribution of displacement. A decrease in $U_{max}$ represents improved control of overall structural deformation, while a decrease in $\Delta U_{joint}$ represents reduced differential movement between adjacent structural blocks. These measures were used to compare deformation responses among the sectional and parametric cases. Rock-mass yielding and local strength reserve were evaluated separately using the Mohr–Coulomb criterion and the point safety factor described in Section 2.4.

## 3. Results

### *3.1. Deformation Response Under Unreinforced and Baseline Pile-Reinforced Conditions*

The displacement distributions of Sections 14–14 and 16–16 under the unreinforced condition and the baseline pile configuration, with a pile spacing of 2.5 m × 2.5 m and pile length of 30 m, are shown in Figures 5–8. The main deformation measures are summarized in Table 2. Deformation in both sections was dominated by vertical settlement, with larger displacements concentrated mainly in the sericitized slate and adjacent structural regions. However, the changes in displacement after pile reinforcement differed markedly between the two sections.

**Table 2.** Deformation measures of the representative sections under unreinforced and baseline pile-reinforced conditions.

| Section | Reinforcement Condition | Maximum Transverse Displacement (mm) | Maximum Vertical Settlement (mm) | Umax (mm) | ΔUjoint (mm) | Reduction in Umax (%) | Reduction in ΔUjoint (%) |
|---|---|---|---|---|---|---|---|
| 14–14 | Unreinforced | 5.46 | 12.0 | 13.1 | 0.475 | – | – |
| 14–14 | 2.5 × 2.5 m piles | 5.57 | 11.7 | 12.7 | 0.460 | 3.1 | 3.2 |
| 16–16 | Unreinforced | 3.90 | 9.70 | 9.70 | 4.70 | – | – |
| 16–16 | 2.5 × 2.5 m piles | 1.64 | 6.43 | 6.43 | 1.93 | 33.7 | 58.9 |

Note: The baseline pile configuration had a spacing of 2.5 m × 2.5 m and a pile length of 30 m.

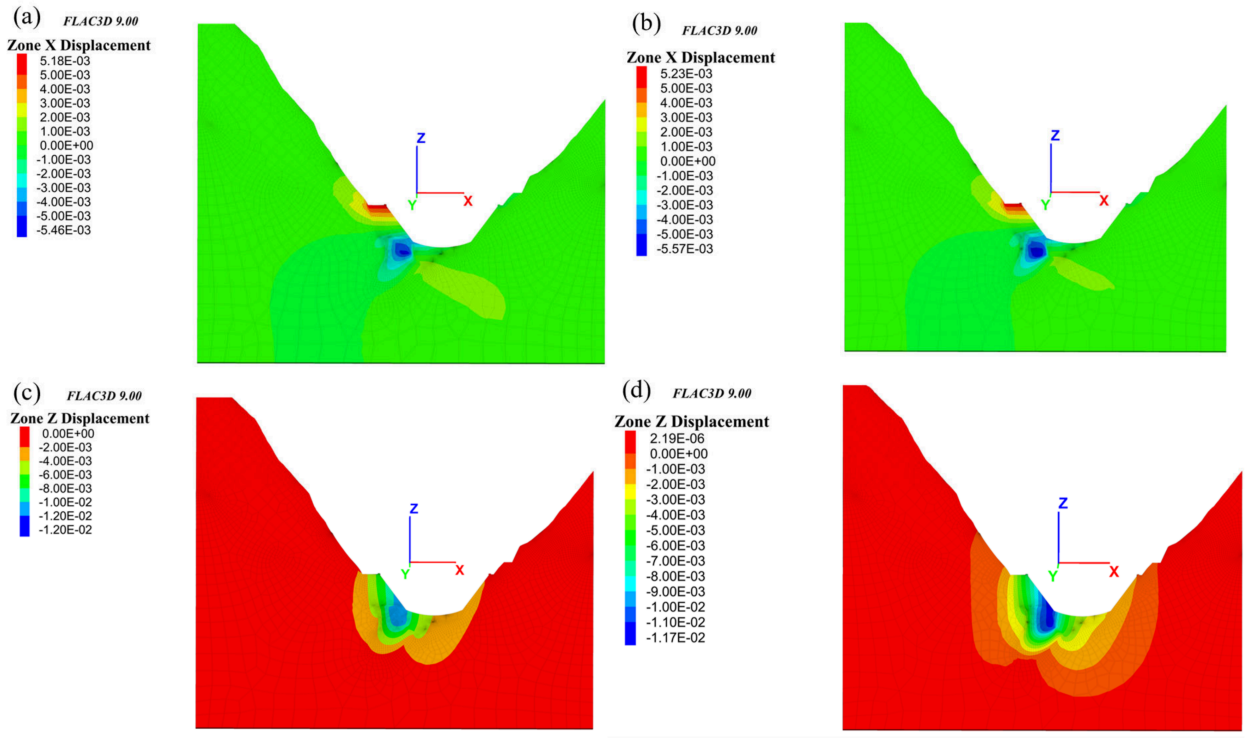


**Figure 5.** Transverse and vertical displacement distributions of Section 14–14 under unreinforced and pile-reinforced conditions. (**a**) Transverse displacement, unreinforced; (**b**) transverse displacement, pile-reinforced; (**c**) vertical displacement, unreinforced; (**d**) vertical displacement, pile-reinforced.

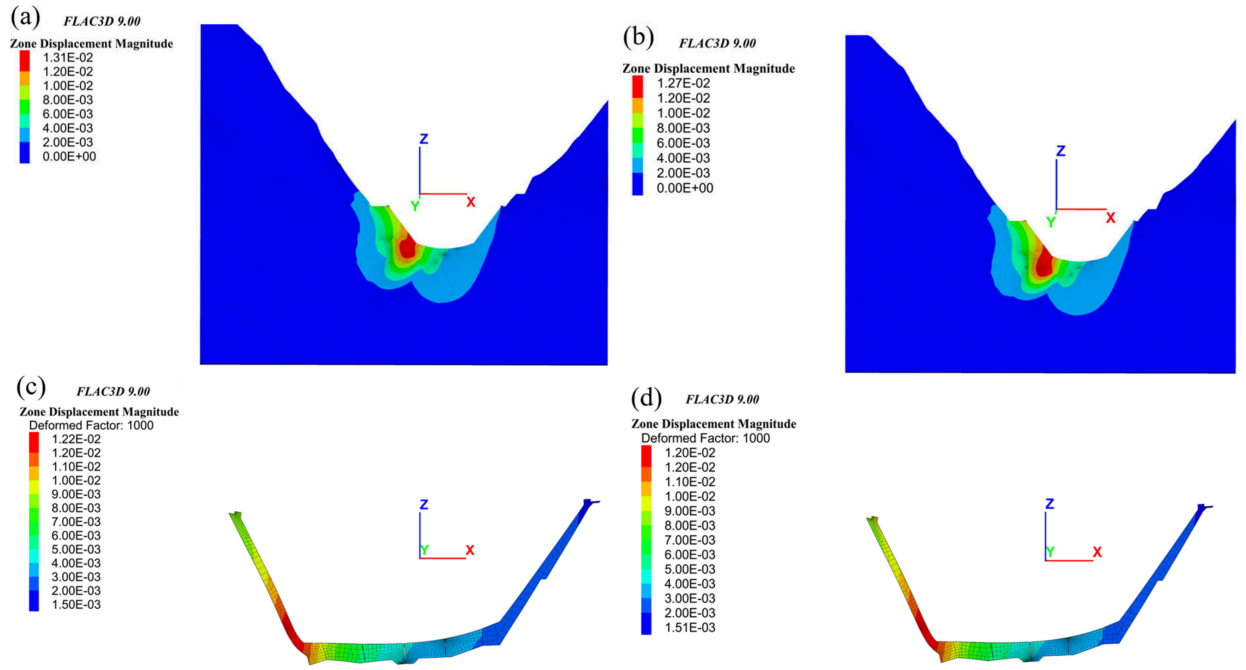


**Figure 6.** Resultant displacement distributions of Section 14–14 under unreinforced and pile-reinforced conditions. (**a**) Resultant displacement, unreinforced; (**b**) resultant displacement, pile-reinforced; (**c**) resultant displacement of the stilling-basin structure, unreinforced; (**d**) resultant displacement of the stilling-basin structure, pile-reinforced.

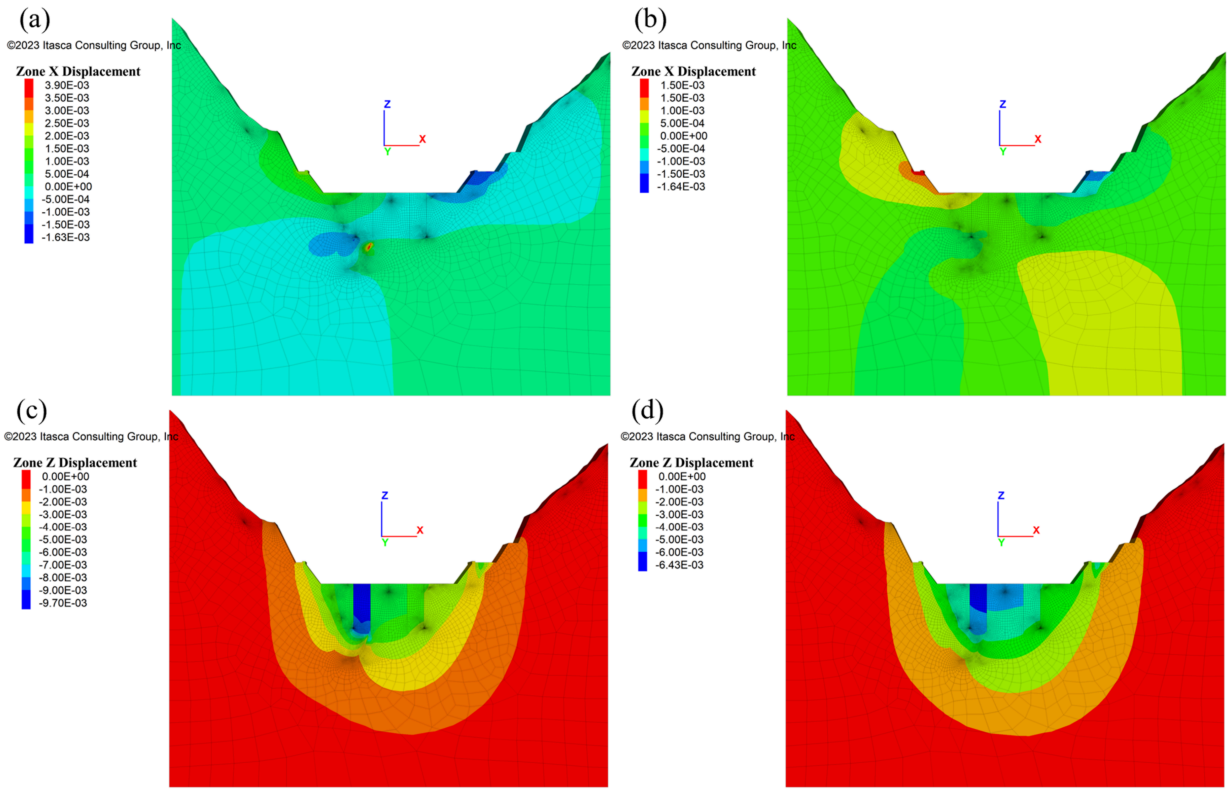


**Figure 7.** Transverse and vertical displacement distributions of Section 16–16 under unreinforced and pile-reinforced conditions. (**a**) Transverse displacement, unreinforced; (**b**) transverse displacement, pile-reinforced; (**c**) vertical displacement, unreinforced; (**d**) vertical displacement, pile-reinforced.

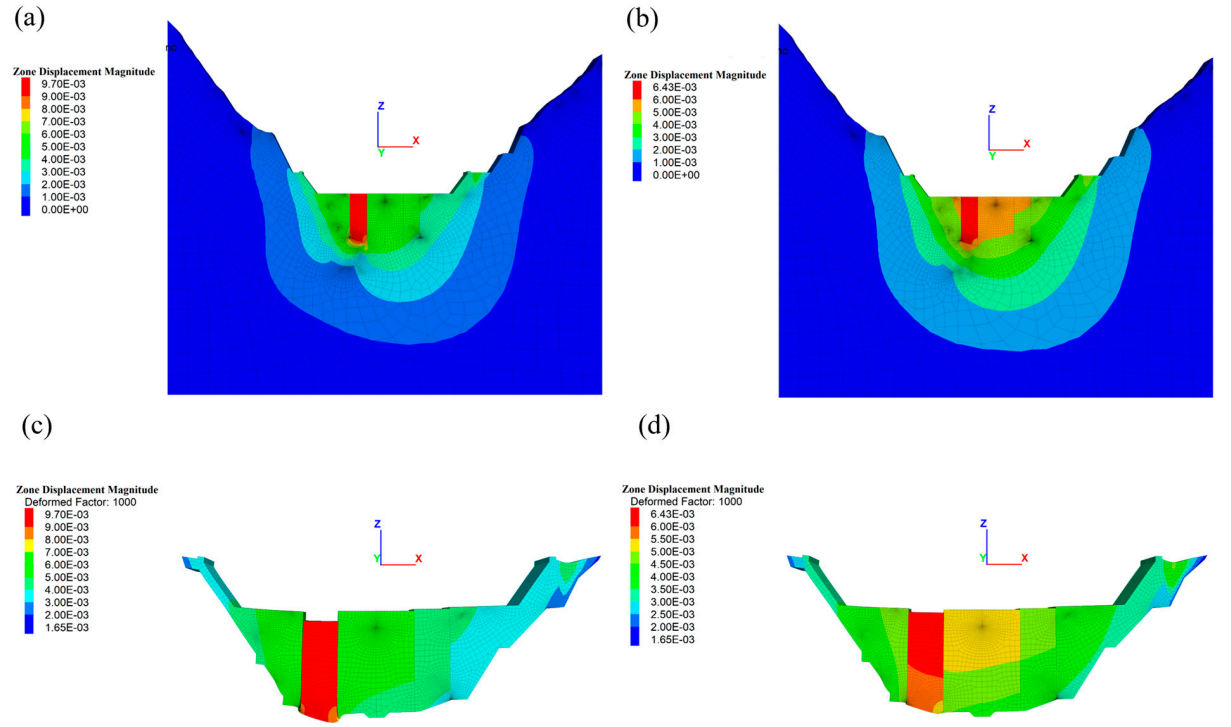


**Figure 8.** Resultant displacement distributions of Section 16–16 under unreinforced and pile-reinforced conditions. (**a**) Resultant displacement, unreinforced; (**b**) resultant displacement, pile-reinforced; (**c**) resultant displacement of the stilling-basin structure, unreinforced; (**d**) resultant displacement of the stilling-basin structure, pile-reinforced.

Under the unreinforced condition, the transverse displacement of Section 14–14 was concentrated mainly in the sericitized slate and the overlying stilling-basin structure, with a maximum value of 5.46 mm (Figure 5a). The maximum vertical settlement was 12.0 mm (Figure 5c), and the maximum resultant displacement, $U_{max}$, was 13.1 mm (Figure 6a). The larger displacement zones were located mainly within the sericitized slate and the adjacent floor slab, particularly along the left sidewall and floor slab at elevations of 1880–1905 m. The maximum vertical joint offset, $\Delta U_{joint}$, was 0.475 mm (Table 2). Under the baseline pile-reinforced condition, the maximum vertical settlement and $U_{max}$ decreased to 11.7 mm and 12.7 mm, respectively (Figures 5d and 6b), while $\Delta U_{joint}$ decreased to 0.460 mm (Table 2). In contrast, the maximum transverse displacement increased slightly from 5.46 mm to 5.57 mm (Figure 5b), and the location of the principal deformation zone remained largely unchanged. Relative to the unreinforced condition, $U_{max}$ and $\Delta U_{joint}$ decreased by approximately 3.1% and 3.2%, respectively. The baseline pile reinforcement therefore produced only modest reductions in the overall and local differential deformation of Section 14–14.

Section 16–16 showed a more pronounced displacement response to pile reinforcement. Under the unreinforced condition, the maximum transverse displacement was 3.90 mm (Figure 7a), while both the maximum vertical settlement and $U_{max}$ were 9.70 mm (Figures 7c and 8a). Larger displacements were concentrated near the end sill above the sericitized slate. The maximum vertical joint offset, $\Delta U_{joint}$, reached 4.70 mm (Table 2). Under the baseline pile-reinforced condition, the maximum transverse displacement decreased to 1.64 mm (Figure 7b), while the maximum vertical settlement and $U_{max}$ both decreased to 6.43 mm (Figures 7d and 8b). Meanwhile, $\Delta U_{joint}$ decreased to 1.93 mm (Table 2). The principal deformation zone remained near the end sill above the sericitized slate, and the maximum resultant displacement occurred close to the junction between the end sill and the left sidewall. Relative to the unreinforced condition, $U_{max}$ and $\Delta U_{joint}$ decreased by 33.7% and 58.9%, respectively. The reduction in local differential deformation was therefore greater than that in the overall deformation magnitude in Section 16–16.

### *3.2. Effects of Pile Spacing on Overall and Local Deformation*

With the pile length fixed at 30 m, the deformation responses were compared for three pile layouts: 2.5 m × 2.5 m, 2.5 m × 5.0 m, and 3.0 m × 3.0 m. The displacement field for the 2.5 m × 2.5 m configuration is presented in Section 3.1. Therefore, Figures 9 and 10 show only the displacement distributions for the 2.5 m × 5.0 m and 3.0 m × 3.0 m configurations, whereas the subsequent quantitative comparison includes all three configurations.

The results for Section 14–14 are shown in Figure 9. The main deformation zones were generally similar under the three pile layouts. Larger displacements were concentrated in the sericitized slate and the adjacent stilling-basin floor, while relatively large structural displacements occurred along the left sidewall and floor slab at elevations of 1880–1905 m. The three configurations differed mainly in displacement magnitude, with no marked shift in the main deformation zones. The $U_{max}$ values for the three pile layouts were 12.7, 12.9, and 12.7 mm, respectively, with a maximum difference of only 0.2 mm. The corresponding maximum vertical settlements were 11.7, 11.8, and 11.7 mm, while the maximum transverse displacements were 5.57, 5.65, and 5.28 mm. The overall deformation magnitude of Section 14–14 remained within a narrow range and showed no consistent trend with pile layout.

Local differential deformation across the structural joints also changed only slightly. The $\Delta U_{joint}$ values were 0.460, 0.459, and 0.481 mm for the 2.5 m × 2.5 m, 2.5 m × 5.0 m, and 3.0 m × 3.0 m pile layouts, respectively. The values for the 2.5 m × 2.5 m and 2.5 m × 5.0 m configurations were nearly identical, whereas that for the 3.0 m × 3.0 m configuration was slightly higher. Although both $U_{max}$ and $\Delta U_{joint}$ varied only slightly among the three configurations,

the two metrics did not follow the same pattern. The 2.5 m × 5.0 m configuration had the largest $U_{max}$, at 12.9 mm, but the smallest $\Delta U_{joint}$, at 0.459 mm.

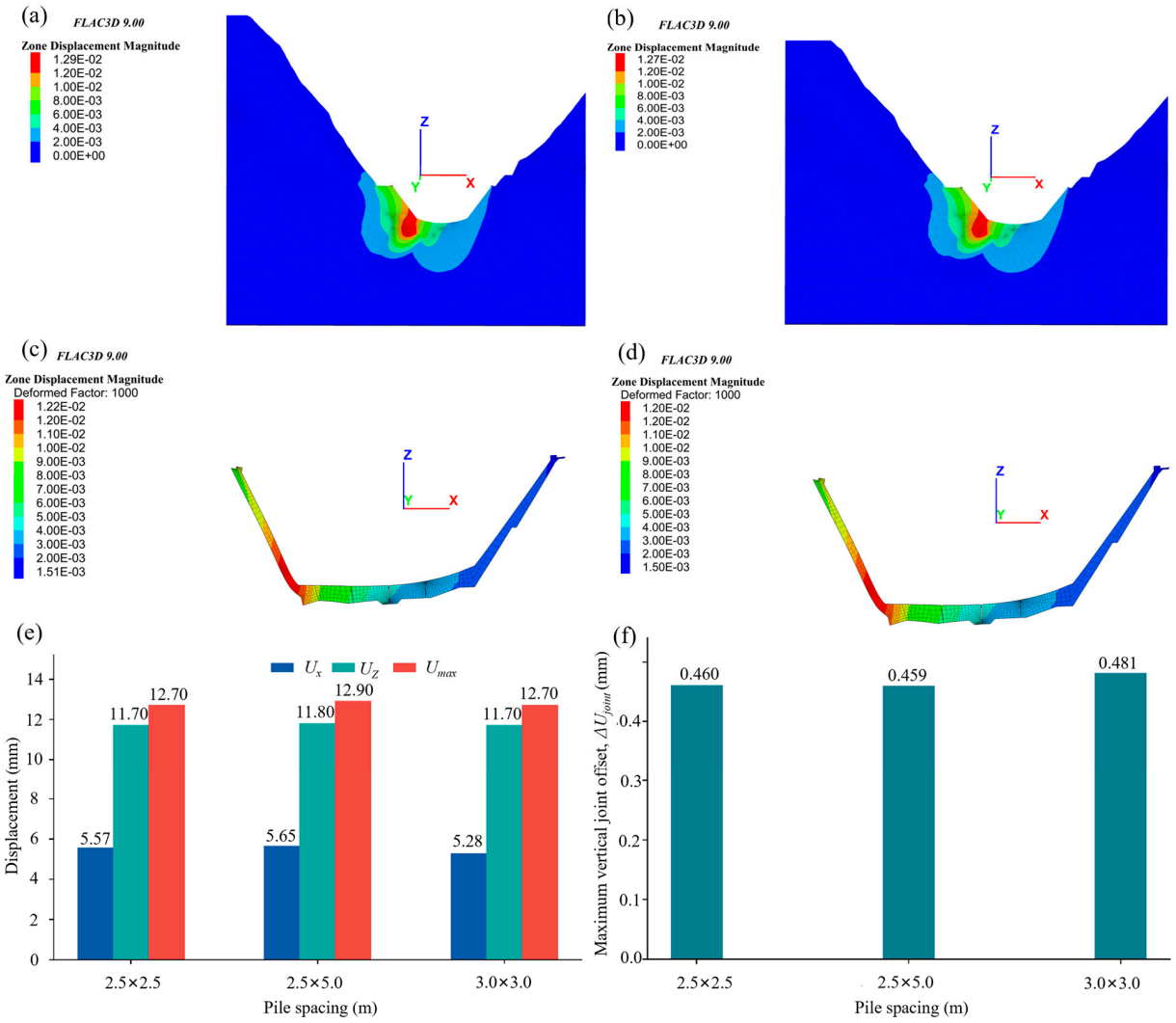


**Figure 9.** Displacement response of Section 14–14 for different pile spacings. (**a**) Resultant displacement, 2.5 m × 5.0 m; (**b**) resultant displacement, 3.0 m × 3.0 m; (**c**) structural resultant displacement, 2.5 m × 5.0 m; (**d**) structural resultant displacement, 3.0 m × 3.0 m; (**e**) maximum transverse, vertical, and resultant displacements under different pile spacings; (**f**) maximum vertical joint offset under different pile spacings.

The results for Section 16–16 are shown in Figure 10. Under all three pile layouts, areas of relatively large resultant displacement were concentrated mainly in the end-sill region above the sericitized slate. For the 2.5 m × 2.5 m configuration, larger settlements were concentrated in the sericitized slate and the overlying end-sill structure, and the maximum resultant displacement occurred near the junction between the end sill and the left sidewall. For the 2.5 m × 5.0 m and 3.0 m × 3.0 m configurations, the location of the maximum vertical settlement shifted to the base of the left-side structural unit, while the maximum resultant displacement remained near the end sill.

For the three pile layouts, the $U_{max}$ values of Section 16–16 were 6.43, 6.71, and 6.75 mm, respectively, with a maximum difference of 0.32 mm. The corresponding maximum vertical settlements were 6.43, 6.71, and 6.75 mm, showing a trend similar to that of $U_{max}$. The maximum transverse displacements were 1.64, 1.64, and 1.63 mm, with a difference of only 0.01 mm among the three cases. The differences in overall displacement among the pile

layouts were therefore mainly associated with vertical settlement and the corresponding resultant displacement, while the transverse displacement remained nearly unchanged.

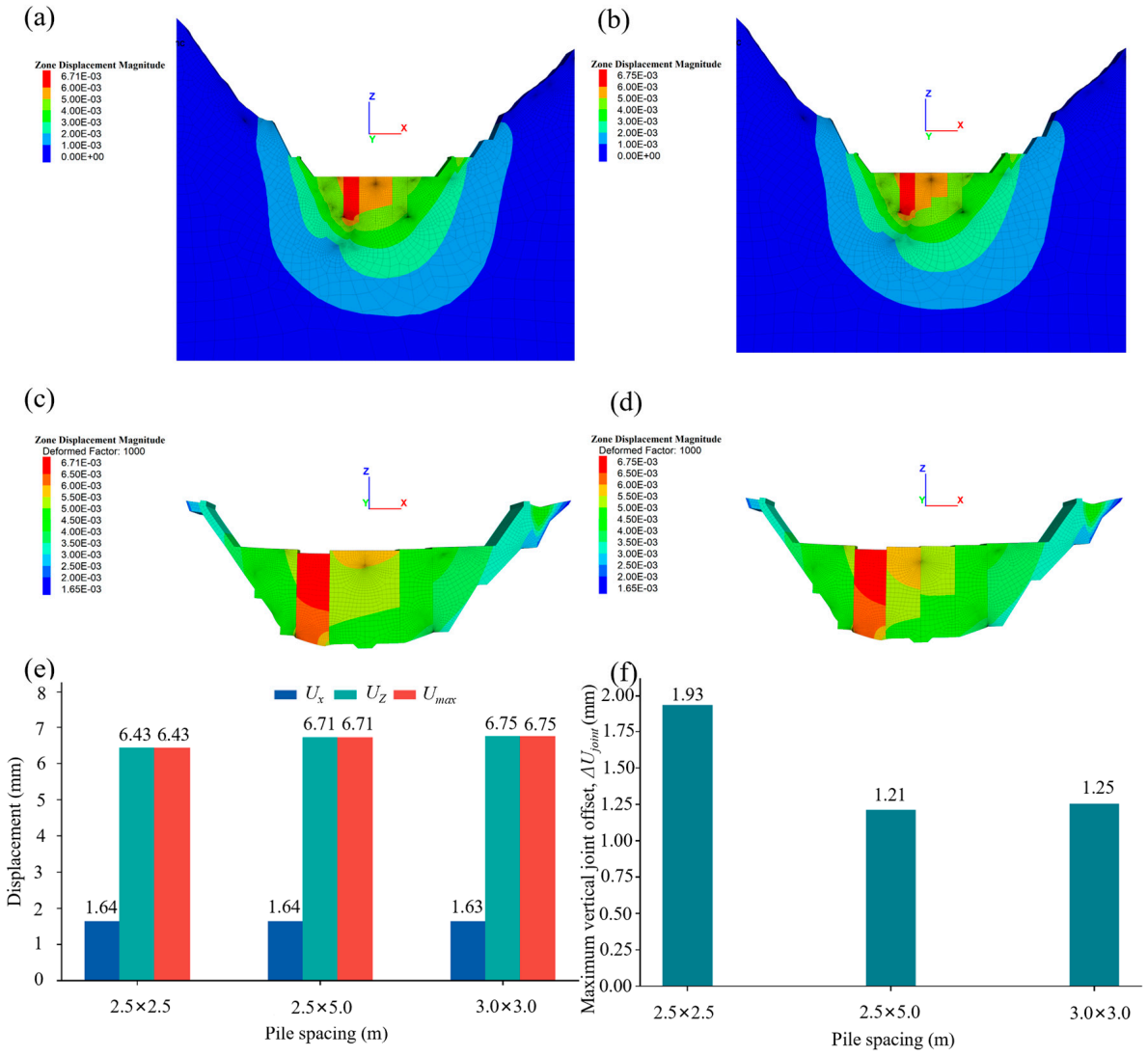


**Figure 10.** Displacement response of Section 16–16 for different pile spacings. (**a**) Resultant displacement, 2.5 m × 5.0 m; (**b**) resultant displacement, 3.0 m × 3.0 m; (**c**) structural resultant displacement, 2.5 m × 5.0 m; (**d**) structural resultant displacement, 3.0 m × 3.0 m; (**e**) maximum transverse, vertical, and resultant displacements under different pile spacings; (**f**) maximum vertical joint offset under different pile spacings.

Compared with the overall deformation magnitude, local differential deformation across the structural joints varied more noticeably with pile layout in Section 16–16. The $\Delta U_{joint}$ values for the three layouts were 1.93, 1.21, and 1.25 mm, respectively. Relative to the baseline 2.5 m × 2.5 m configuration, $\Delta U_{joint}$ decreased by approximately 37.3% and 35.2% for the 2.5 m × 5.0 m and 3.0 m × 3.0 m configurations, whereas $U_{max}$ increased by approximately 4.4% and 5.0%, respectively. Among the three layouts, the 2.5 m × 2.5 m configuration had the smallest $U_{max}$, whereas the 2.5 m × 5.0 m configuration had the smallest $\Delta U_{joint}$. The two metrics therefore responded differently to pile layout.

### *3.3. Effects of Pile Length on Overall and Local Deformation*

With the pile spacing fixed at 3.0 m × 3.0 m, the deformation response of Section 14–14 was compared for pile lengths of 15, 20, 25, and 30 m. The displacement distributions

for the 30 m pile length are presented in Figure 9b,d. Figures 11–13 therefore show the resultant displacement and structural resultant displacement for pile lengths of 15, 20, and 25 m, while all four pile lengths are included in the quantitative comparison.

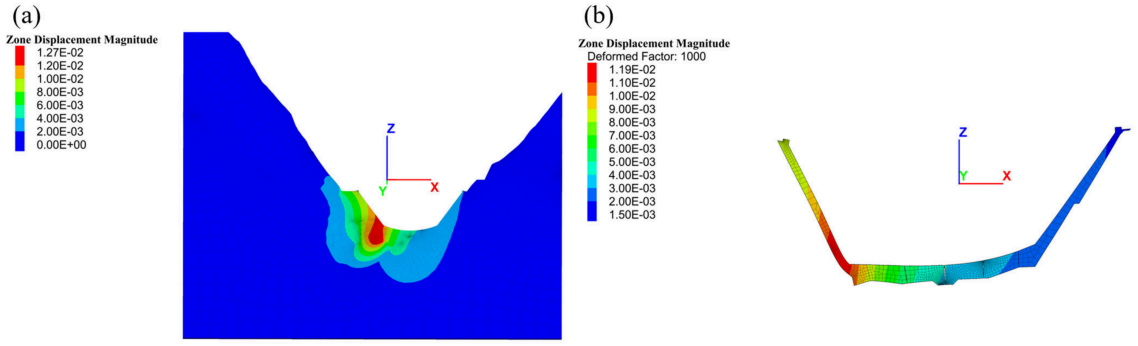


**Figure 11.** Displacement response of Section 14–14 for a pile length of 15 m. (**a**) Resultant displacement; (**b**) structural resultant displacement.

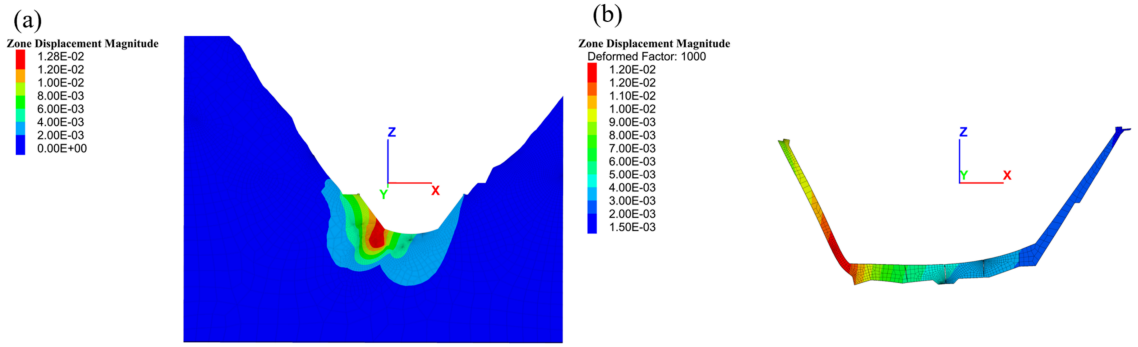


**Figure 12.** Displacement response of Section 14–14 for a pile length of 20 m. (**a**) Resultant displacement; (**b**) structural resultant displacement.

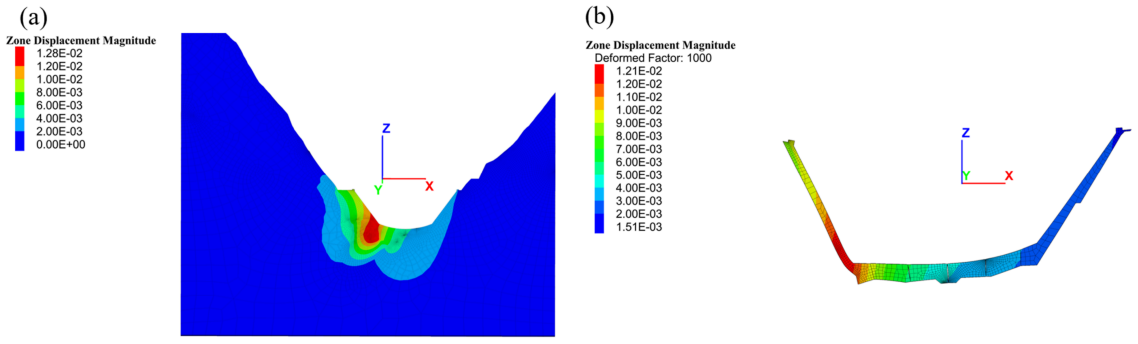


**Figure 13.** Displacement response of Section 14–14 for a pile length of 25 m. (**a**) Resultant displacement; (**b**) structural resultant displacement.

For all four pile lengths, the principal deformation zones remained within the sericitized slate and the adjacent floor slab, with relatively large structural displacements along the left sidewall and the floor slab at elevations of 1880–1905 m. No marked shift in these zones occurred as the pile length increased from 15 to 30 m.

For pile lengths of 15, 20, 25, and 30 m, the corresponding $U_{max}$ values were 12.7, 12.8, 12.8, and 12.7 mm, respectively, with a maximum difference of only 0.1 mm. The maximum vertical settlement ranged from 11.6 to 11.8 mm, while the maximum transverse displacement ranged from 5.28 to 5.40 mm. Thus, the overall deformation magnitude remained within a narrow range, and $U_{max}$ showed no monotonic trend with increasing pile length.

The maximum vertical joint offsets, $\Delta U_{joint}$, were 0.462, 0.463, 0.472, and 0.481 mm for pile lengths of 15, 20, 25, and 30 m, respectively. The values for the 15 and 20 m piles were nearly identical, followed by a slight increase for the 25 and 30 m piles. From 15 to 30 m, $\Delta U_{joint}$ increased by 0.019 mm, or approximately 4.1%, while $U_{max}$ remained at 12.7 mm. Increasing pile length from 15 to 30 m produced little change in overall deformation and did not reduce the joint offset.

### *3.4. Deformation Response to Variations in Weak-Rock Foundation Conditions*

With the structural configuration and loading conditions kept unchanged, the displacement responses were compared for different thicknesses of competent rock overlying the sericitized slate and for different deformation moduli of the weak rock. The effect of overlying competent-rock thickness was examined using Section 14–14, whereas the effect of weak-rock deformation modulus was evaluated for both Sections 14–14 and 16–16. All cases were analyzed under unreinforced conditions to isolate the deformation response associated with changes in the weak-rock foundation conditions.

#### 3.4.1. Effects of Overlying Competent-Rock Thickness

The spatial distribution of displacement in Section 14–14 was generally similar for overlying competent rock thicknesses of 5, 10, 15, and 20 m. In all cases, the main deformation zones were located within the sericitized slate and the adjacent stilling basin structure. The maximum transverse displacements were 5.20, 5.18, 5.16, and 5.13 mm, respectively, while the corresponding maximum vertical settlements were 12.0, 11.9, 12.0, and 12.1 mm. The $U_{max}$ values were 12.6, 12.5, 12.7, and 12.7 mm, with a maximum difference of only 0.2 mm (Figure 14a). The variation in overall deformation among the four thickness conditions was therefore small.

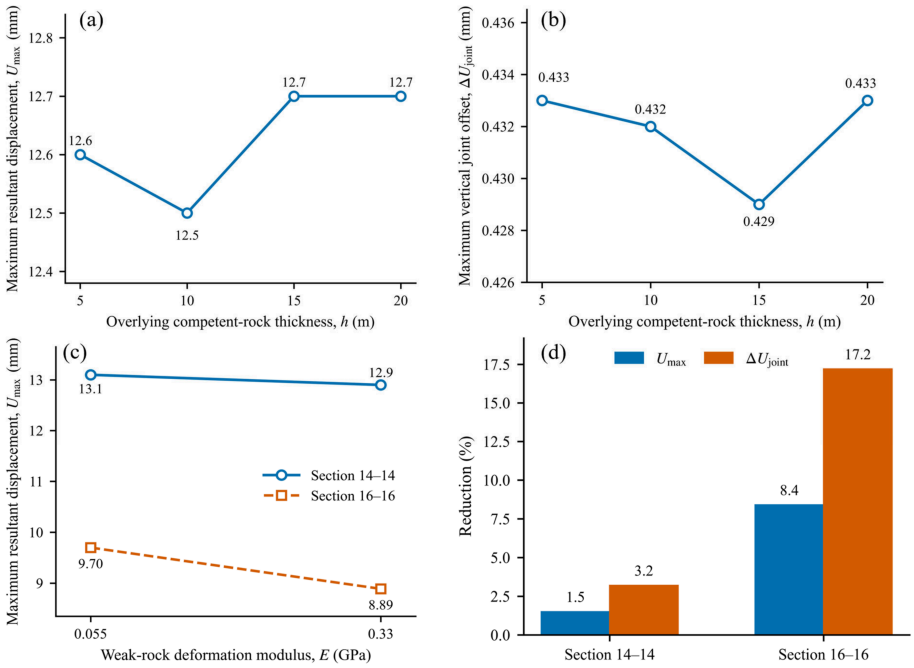


**Figure 14.** Deformation responses under varying weak-rock foundation conditions. (**a**) Maximum resultant displacement at different overlying competent-rock thicknesses; (**b**) maximum vertical joint offset at different overlying competent-rock thicknesses; (**c**) maximum resultant displacement at different weak-rock deformation moduli; and (**d**) reductions in maximum resultant displacement and joint offset associated with the increase in weak-rock deformation modulus.

The maximum vertical joint offsets, $\Delta U_{joint}$, were 0.433, 0.432, 0.429, and 0.433 mm, respectively, with a maximum difference of only 0.004 mm (Figure 14b). The minimum $U_{max}$ occurred for the 10 m case, whereas the minimum $\Delta U_{joint}$ occurred for the 15 m case. Both deformation measures varied only slightly as the overlying competent rock thickness increased from 5 to 20 m, and neither exhibited a monotonic trend.

#### 3.4.2. Effects of Weak-Rock Deformation Modulus

When the deformation modulus of the sericitized slate was increased from 0.055 to 0.33 GPa, the displacement magnitudes decreased in both Sections 14–14 and 16–16, although the reductions differed between the two sections. The principal deformation zones in each section remained generally unchanged under the two deformation-modulus conditions.

For Section 14–14, the maximum transverse displacement decreased from 5.46 to 5.15 mm, while the maximum vertical settlement decreased from 12.0 to 11.8 mm. $U_{max}$ decreased from 13.1 to 12.9 mm, corresponding to a reduction of 0.2 mm, or approximately 1.5%. Meanwhile, $\Delta U_{joint}$ decreased from 0.475 to approximately 0.460 mm. The main deformation remained concentrated in the sericitized slate and the adjacent stilling-basin floor.

For Section 16–16, the maximum transverse displacement decreased from 3.90 to 1.79 mm. Both the maximum vertical settlement and $U_{max}$ decreased from 9.70 to 8.89 mm. The reduction in $U_{max}$ was 0.81 mm, or approximately 8.4%. $\Delta U_{joint}$ decreased from 4.70 to 3.89 mm, corresponding to a reduction of approximately 17.2%. The main deformation zone remained in the end-sill region above the sericitized slate and the adjacent structural area.

The increase in weak-rock deformation modulus produced larger reductions in both $U_{max}$ and $\Delta U_{joint}$ in Section 16–16 than in Section 14–14 (Figure 14c,d). In both sections, the principal deformation zones remained in approximately the same locations.

### *3.5. Foundation-Rock Yielding and Pile-Concrete Stresses*

Under the check-flood condition, plastic yielding was confined to localized parts of the upper sericitized slate zone (Figure 15a). Most sericitized slate zones had point safety factors greater than 1.10. Values approaching 1.0 occurred mainly near the sidewall and the localized plastic zones, and zones with point safety factors below 1.05 occupied only a limited area (Figure 15b). The relatively large displacement in Section 14–14 coincided with localized yielding in the sericitized slate foundation, while most rock zones remained within the Mohr–Coulomb yield surface.

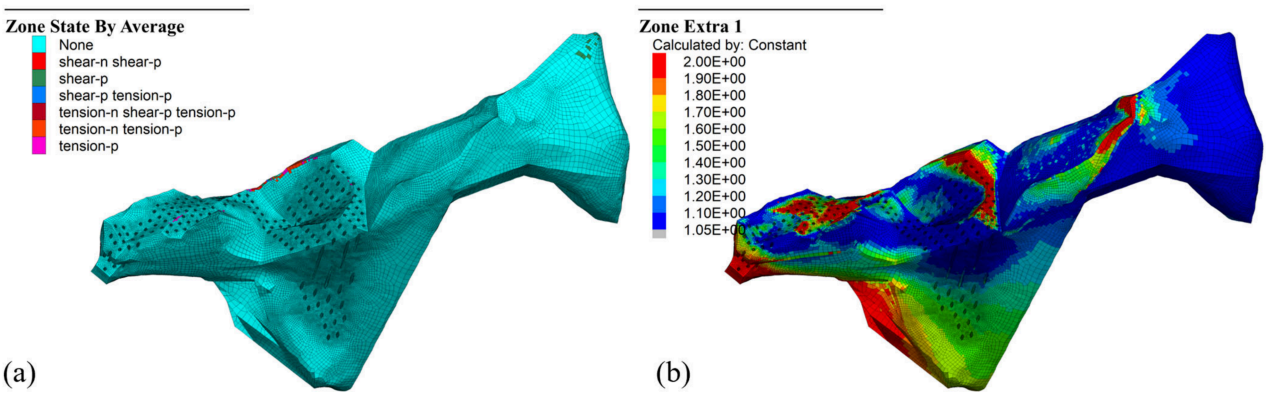


**Figure 15.** Yielding response of the sericitized slate foundation under the check-flood condition. (**a**) Distribution of plastic zones; (**b**) distribution of the point safety factor.

The reinforcing piles were predominantly subjected to compression under the check-flood condition. Compressive stress remained below approximately 5.0 MPa throughout most of the pile zones. Local stress concentrations occurred near the pile heads and toes,

where the maximum compressive stress reached 8.95 MPa. This peak value corresponded to 62.6% of the design compressive strength of C30 concrete, 14.3 MPa. The calculated compressive stresses in the piles remained below the concrete design strength.

## 4. Discussion

### 4.1. Location-Dependent Performance of Pile Reinforcement

The baseline cases for Sections 14–14 and 16–16 used the same pile spacing and length, but differed in pile embedment and in the structural components supported by the piles. In Section 14–14, the piles were installed beneath the central floor slab, where the sericitized slate extended laterally and varied in burial depth. The resulting changes in $U_{max}$ and $\Delta U_{joint}$ were modest, and the principal deformation zone remained largely unchanged after reinforcement. Section 16–16 intersected the end sill, adjacent structural blocks, structural joints, and the underlying weak rock. At this location, pile reinforcement produced larger reductions in both overall deformation and vertical joint offset.

The contrast between the two sections is associated with differences in weak rock geometry, the rock units crossed by the piles, pile embedment, and the overlying structural configuration [12,22,34–38]. Because these characteristics varied simultaneously, the observed difference cannot be attributed to pile spacing or pile length alone. Pile-reinforcement performance in a heterogeneous rock foundation therefore depends on the local embedment and structural conditions under which the piles operate.

### 4.2. Different Responses of Overall and Local Deformation

The maximum resultant displacement and the maximum vertical joint offset responded differently to pile reinforcement and changes in pile configuration. In Section 16–16, the baseline pile reinforcement produced a larger relative reduction in $\Delta U_{joint}$ than in $U_{max}$. The pile-spacing analysis showed a similar distinction: the 2.5 m × 2.5 m layout produced the smallest $U_{max}$, whereas the 2.5 m × 5.0 m layout produced the smallest $\Delta U_{joint}$. In the pile-length analysis for Section 14–14, $U_{max}$ remained within a narrow range, while $\Delta U_{joint}$ increased slightly with pile length. These results consistently show that a change in pile configuration can affect overall structural deformation and local joint movement differently.

This difference arises from the quantities represented by the two measures. $U_{max}$ records the largest resultant displacement within the concrete stilling-basin structure, regardless of its location, whereas $\Delta U_{joint}$ records the relative vertical movement between corresponding points on adjacent structural blocks. A change in load transfer may therefore alter the movement of individual blocks and their relative displacement without producing a comparable change in the maximum displacement of the entire structure. Conversely, a reduction in $U_{max}$ does not necessarily indicate a corresponding reduction in joint movement. For a stilling basin divided by structural joints, considering both measures distinguishes overall deformation control from local deformation compatibility and provides a more complete comparison of pile configurations [19,20,39–41].

### 4.3. Effects of Pile Configuration on Deformation-Control Performance

The three pile layouts produced only small differences in $U_{max}$ at both representative sections, whereas $\Delta U_{joint}$ in Section 16–16 was more sensitive to the plan arrangement. Increasing pile density therefore did not improve overall and local deformation control to the same extent. Once pile reinforcement was introduced, changes in plan layout had a limited influence on the maximum overall displacement but could still modify differential movement between adjacent structural blocks. This distinction further indicates that pile-layout performance depends on the deformation measure considered [42,43].

The pile-length analysis showed a similarly non-monotonic response. In Section 14–14, with the pile spacing fixed at 3.0 m × 3.0 m, $U_{max}$ remained within 12.7–12.8 mm as the pile length increased from 15 to 30 m, while $\Delta U_{joint}$ increased slightly from 0.462 to 0.481 mm. Within the investigated range, increasing pile length produced little change in overall deformation and did not reduce local joint movement. Increasing pile length alone therefore did not provide further deformation control under the structure–foundation conditions represented by Section 14–14 [44,45].

The piles had a diameter of 1.0 m. The 2.5 m × 2.5 m, 2.5 m × 5.0 m, and 3.0 m × 3.0 m layouts therefore corresponded to transverse and longitudinal spacing-to-diameter ratios of 2.5 and 2.5, 2.5 and 5.0, and 3.0 and 3.0, respectively. Within this set of rectangular layouts, the configuration associated with the smallest $U_{max}$ was not consistently the configuration associated with the smallest $\Delta U_{joint}$. No single spacing-to-diameter ratio among the examined cases therefore minimized both deformation measures. A broader set of spacing combinations, including intermediate and staggered layouts, would be needed to identify an optimum spacing-to-diameter ratio.

### 4.4. Influence of Weak-Rock Foundation Conditions on Deformation Response

The geometry and deformation modulus of the sericitized slate affected the stilling-basin response differently. In Section 14–14, varying the thickness of competent rock overlying the weak rock from 5 to 20 m produced only small changes in $U_{max}$ and $\Delta U_{joint}$. Increasing the deformation modulus of the sericitized slate, however, reduced both measures, with a larger reduction in Section 16–16 than in Section 14–14. Within the investigated parameter ranges, the structural response was therefore more sensitive to the change in weak-rock stiffness than to the local thickness of the overlying competent rock.

The limited influence of overlying competent-rock thickness is consistent with the irregular geometry of the sericitized slate. The weak rock does not form a continuous horizontal layer; its lateral extent, burial depth, and contacts with the surrounding rock vary across the foundation. In the parametric analysis, its overall position and lateral extent were retained while only the local thickness of the overlying competent rock was varied. This change did not substantially alter the principal deformation zones. The geometric influence of the weak rock is therefore related to its overall spatial configuration and its contact with the surrounding rock masses, rather than to the overlying thickness alone [5].

The response to weak-rock deformation modulus also differed between the two structural locations. Increasing the modulus from 0.055 to 0.33 GPa reduced $U_{max}$ by approximately 1.5% in Section 14–14 and 8.4% in Section 16–16. In Section 16–16, $\Delta U_{joint}$ also decreased by approximately 17.2%. Although the deformation magnitudes decreased, the principal deformation zones remained in approximately the same locations. The effect of weak-rock stiffness therefore depended on the spatial relationship among the sericitized slate, the surrounding competent rock, and the overlying structural components [3]. As these analyses used the unreinforced models, they characterize the baseline response of the structure–foundation system to variations in weak-rock geometry and stiffness.

### 4.5. Engineering Implications and Study Limitations

The results indicate that pile arrangements for large stilling basins founded on heterogeneous weak rock foundations should be evaluated in relation to the local foundation profile and the structural components supported by the piles. At locations where weak rock and structural joints occur together, the governing deformation response may differ from that in other parts of the same structure. Considering $U_{max}$ together with $\Delta U_{joint}$ allows the overall deformation of the stilling basin and the differential movement between adjacent blocks to be evaluated separately. Accordingly, pile spacing and length should be

assessed for individual structural locations rather than transferred unchanged across the entire foundation.

The analyses covered two transverse sections, three rectangular pile layouts, and the mapped weak rock geometry of the Kala stilling basin. The conclusions are therefore specific to the investigated structural geometry, foundation conditions, parameter ranges, and check-flood loading condition. Application to other hydraulic structures should account for differences in structural dimensions, geological profiles, hydraulic loading, and pile–foundation interaction. Analyses of additional sections, intermediate or staggered pile layouts, and alternative weak-rock boundary geometries would be required to determine whether the spatial differences observed in this study persist beyond the investigated cases.

The principal mapped geological structures were represented explicitly, whereas the surrounding rock masses were described using an isotropic Mohr–Coulomb model. Smaller joint sets, directional anisotropy, and strain-softening behavior were not represented explicitly. The model therefore captures engineering-scale deformation associated with the mapped weak rock and major geological structures, but does not reproduce block-scale kinematics or progressive failure along individual discontinuities. The shared-node treatment at the pile–rock boundary represents a fully bonded condition and excludes local slip and separation. It may therefore produce a stiffer pile–rock response than a model with an explicit interface. The deformation results are interpreted within this assumption and are not used to determine the limiting pile–rock interface resistance. The structural joints between adjacent concrete blocks were represented by interface elements, and the calculated joint movements may depend on the adopted interface parameters and local mesh discretization.

The loading considered in this study was quasi-static and corresponded to the check-flood condition. Transient hydrodynamic or seismic loading would involve additional inertia, fluid–structure interaction, pore-pressure changes, and different pile–foundation load-transfer mechanisms [46]. Under the analyzed check-flood condition, rock-mass yielding and local strength reserve were characterized using the Mohr–Coulomb yielding response and the point safety factor, respectively. The results showed localized yielding and locally reduced strength reserve rather than widespread yielding throughout the sericitized slate foundation. Strain-based criteria provide a complementary means of evaluating the onset of rock-mass failure [47,48], but their application requires critical-strain values determined for sericitized slate under representative confinement and moisture conditions.

## 5. Conclusions

This study investigated the deformation-control performance of pile reinforcement for a large stilling basin founded on a heterogeneous weak-rock foundation using three-dimensional numerical analysis under the check-flood condition. The effects of structural location, pile configuration, and weak-rock conditions on the structural response were compared. The main conclusions are as follows:

(1) Pile reinforcement produced different deformation reductions at the two representative sections. Both baseline cases used a pile spacing of 2.5 m × 2.5 m and a pile length of 30 m. In Section 14–14, $U_{max}$ and $\Delta U_{joint}$ decreased by approximately 3.1% and 3.2%, respectively, whereas the corresponding reductions in Section 16–16 were approximately 33.7% and 58.9%. The contrasting responses were associated with differences in weak-rock distribution, pile embedment conditions, and the structural components supported by the piles.

(2) Overall deformation and local differential deformation did not respond consistently to changes in pile configuration. In Section 16–16, the 2.5 m × 2.5 m pile layout produced the smallest $U_{max}$, whereas the minimum $\Delta U_{joint}$ occurred under the 2.5 m × 5.0 m

layout. The two measures describe different aspects of the structural response and should be considered together when comparing pile arrangements for a stilling basin divided by structural joints.

(3) Changes in plan layout and pile length did not produce systematic reductions in both deformation measures. In Section 16–16, $U_{max}$ varied only from 6.43 to 6.75 mm among the different pile layouts. In Section 14–14, $U_{max}$ remained within 12.7–12.8 mm as the pile length increased from 15 to 30 m, while $\Delta U_{joint}$ increased slightly. Within the investigated parameter ranges, neither a denser layout nor a longer pile consistently improved both overall and local deformation control.

(4) Changes in overlying competent-rock thickness and weak-rock deformation modulus affected structural deformation differently. In Section 14–14, increasing the thickness of competent rock overlying the weak rock from 5 to 20 m produced only small changes in both overall deformation and joint offset. When the deformation modulus of the weak rock increased from 0.055 to 0.33 GPa, deformation decreased in both Sections 14–14 and 16–16, with a stronger response in Section 16–16. In contrast, varying the overlying competent rock thickness from 5 to 20 m in Section 14–14 produced only minor changes in both deformation measures.

**Author Contributions:** Conceptualization, L.Y., W.W., and K.Z.; methodology, M.J. and Q.M.; software, W.L.; validation, L.Y., W.W. and M.J.; formal analysis, K.Z., Q.M.; investigation, W.L.; resources, L.Y.; data curation, L.Y., Q.M.; writing—original draft preparation, L.Y.; writing—review and editing, K.Z.; visualization, Q.M.; supervision, W.W.; project administration, L.Y.; funding acquisition, K.Z. All authors have read and agreed to the published version of the manuscript.

**Funding:** This research was funded by the State Key Laboratory of Hydraulic Engineering Intelligent Construction and Operation, Tianjin University (grant number HESS-2617) and the Fundamental Research Funds for the Central Universities (grant number B260201078).

**Data Availability Statement:** The data presented in this study are available on request from the corresponding author. The data are not publicly available due to confidentiality restrictions associated with the engineering project.

**Conflicts of Interest:** Authors Liang Yin, Weiwei Wu, Ming Jiang, and Wei Li were employed by PowerChina Huadong Engineering Corporation, and this employment relationship has been explicitly disclosed. The remaining authors declare that no commercial or financial relationships existed that could be construed as a potential conflict of interest.

## References

1. Hoek, E.; Brown, E.T. Practical estimates of rock mass strength. *Int. J. Rock Mech. Min. Sci.* **1997**, *34*, 1165–1186. [CrossRef]
2. Jing, L. A review of techniques, advances and outstanding issues in numerical modelling for rock mechanics and rock engineering. *Int. J. Rock Mech. Min. Sci.* **2003**, *40*, 283–353. [CrossRef]
3. Shao, C.F.; Xu, Y.X.; Chen, J.; Zheng, S.; Gu, H.; Qin, X.N. Numerical analysis method of equivalent deformation parameters for grouted arch dam abutment fractured rock masses considering scale effects and anisotropy. *Comput. Geotech.* **2024**, *165*, 105929. [CrossRef]
4. Stead, D.; Eberhardt, E.; Coggan, J.S. Developments in the characterization of complex rock slope deformation and failure using numerical modelling techniques. *Eng. Geol.* **2006**, *83*, 217–235. [CrossRef]
5. Zhao, J.S.; Chen, B.R.; Jiang, Q.; Xu, D.P.; He, B.G.; Duan, S.Q. In-situ comprehensive investigation of deformation mechanism of the rock mass with weak interlayer zone in the Baihetan hydropower station. *Tunn. Undergr. Space Technol.* **2024**, *148*, 105690. [CrossRef]
6. Gimenes, E.; Fernández, G. Hydromechanical analysis of flow behavior in concrete gravity dam foundations. *Can. Geotech. J.* **2006**, *43*, 244–259. [CrossRef]
7. Zhang, Q.H.; Shi, G.H. Verification of a DDA-based hydro-mechanical model and its application to dam foundation stability analysis. *Int. J. Rock Mech. Min. Sci.* **2021**, *138*, 104627. [CrossRef]

8. Zhang, X.J.; Benamar, A.; Luo, Y.L. Experimental study on contact erosion at the interface between the weak interlayer and the crushed zone. *Geomech. Energy Environ.* **2023**, *36*, 100492. [CrossRef]
9. Li, L.; Chen, T.; Liu, H.; Guo, R.; He, R.; Meng, Q. Coupled LEM–CZM Numerical Framework for Landslide Simulation and Its Application to Geotechnical Design. *Designs* **2025**, *9*, 133. [CrossRef]
10. de Sanctis, L.; Russo, G. Analysis and performance of piled rafts designed using innovative criteria. *J. Geotech. Geoenvironmental Eng.* **2008**, *134*, 1118–1128. [CrossRef]
11. Chen, Y.F.; Ai, Z.Y.; Ma, Z.G.; Ye, Z.K.; Mao, X.B. Time-dependent behavior of vertically loaded rock-socketed piles in multilayered saturated viscoelastic rock-soil mass. *Comput. Geotech.* **2024**, *172*, 106438. [CrossRef]
12. Chen, Y.F.; Ai, Z.Y.; Ma, Z.G.; Ye, Z.K. Vertical performance of rock-socketed pile group in layered saturated rock-soil mass. *Comput. Geotech.* **2023**, *157*, 105322. [CrossRef]
13. Murali, A.K.; Haque, A.; Bui, H.H. Advancing Rock-Socketed Pile Design with a Unified Interface Shear Strength Framework for Soft Rocks. *Rock Mech. Rock Eng.* **2024**, *57*, 7253–7269. Correction in *Rock Mech. Rock Eng.* **2024**, *57*, 8923. https://doi.org/10.1007/s00603-024-03918-2. [CrossRef]
14. Zhang, Y.J.; Bai, X.Y.; Yan, N.; Sang, S.K.; Liu, J.W.; Zhang, Y.M. Load transfer characteristics of rock-socketed bored piles under dynamic compaction in reclaimed areas. *Ocean Eng.* **2024**, *311*, 118924. [CrossRef]
15. Wei, Y.J.; Zhao, M.Y.; Zeng, Y.; Yang, Y.Y.; Liu, H.C.; Li, J.G.; Jie, Y.X. Bearing behaviors of rock-socketed piles in layered dynamically compacted soil-rock mixtures: A case study. *Alex. Eng. J.* **2025**, *114*, 12–29. [CrossRef]
16. So, A.K.O. Performance of high capacity socketed H-piles with long rock socket. *Soils Found.* **2024**, *64*, 101481. [CrossRef]
17. Zhao, X.M.; Yan, N.; Bai, X.Y.; Sang, S.K.; Chen, X.Y.; Zhang, Y.M.; Zhang, M.Y. Vertical compressive bearing performance and optimization design method of large-diameter manually-excavated rock-socketed cast-in-place piles. *Sci. Rep.* **2023**, *13*, 14234. [CrossRef]
18. Zhang, P.; Jin, H.; Guo, R.; Xu, X.; Li, S.; Meng, Q. Optimization of the Prestress Value for Multi-Row Anchor in Anti-Slide Pile Based on a Staged Orthogonal Design. *Designs* **2025**, *9*, 142. [CrossRef]
19. Luo, R.P.; Li, Z.D.; Zhu, B.T.; Yang, Q.J. Differential settlements of piled raft foundation: Numerical simulations, empirical equations and design charts. *J. Build. Eng.* **2025**, *111*, 113118. [CrossRef]
20. Modak, R.; Singh, B. Time-dependent performance of large piled raft in clayey soil. *Ocean Eng.* **2024**, *303*, 117839. [CrossRef]
21. Chen, Y.F.; Ai, Z.Y.; Ma, Z.G.; Ye, Z.K. Interaction Between Layered Saturated Soft Rock-Soil Mass and Pile Groups Considering Free-Standing Length and Rock-Socketed Depth. *Int. J. Numer. Anal. Methods Geomech.* **2025**, *49*, 2805–2819. [CrossRef]
22. Qin, Z.C.; Bai, X.Y.; Yin, J.C.; Yan, N.; Zhao, X.M.; Zhang, Y.M. Axial bearing behavior of rock-socketed piles in overlying thick fill-underlying soft rock strata under coastal engineering conditions. *Ocean Eng.* **2026**, *347*, 124010. [CrossRef]
23. Mathumidah, K.; Tran, K.M.; Haque, A.; Bui, H. Effects of Weak-Interface Materials on the Axial Load Capacity of Rock-Socketed Piles: A Numerical Investigation. *Rock Mech. Rock Eng.* **2025**, *58*, 13369–13392. [CrossRef]
24. Zhou, Y.J.; Tan, L.H.; Yue, Z.L.; Yan, L.; Jiang, K.Y.; Gou, X.Y. The Vertical Behaviors of Dissimilar Pile Composite Foundations over Inclined Bedrock. *Buildings* **2024**, *14*, 424. [CrossRef]
25. Li, Z.; Ding, Y.Z.; Huang, S.Y.; Cai, L.B.; Wang, J.J. Asymmetric mechanical responses of CFG Pile composite foundations in inclined strata. *Transp. Geotech.* **2026**, *64*, 102225. [CrossRef]
26. Leung, Y.F.; Lo, M.K. Probabilistic assessment of pile group response considering superstructure stiffness and three-dimensional soil spatial variability. *Comput. Geotech.* **2018**, *103*, 193–200. [CrossRef]
27. Zhang, W.Y.; Shi, J.K.; Lin, G.M.; Lin, C. Settlement Analysis of a Large Pile Group Supporting an LNG Storage Tank. *Int. J. Numer. Anal. Methods Geomech.* **2025**, *49*, 3858–3879. [CrossRef]
28. Liang, R.; Yin, Z.Y.; Yin, J.H.; Wu, P.C.; Chen, Z.J. An enhanced micromechanical rock-pile interface model with application to rock-socketed pile modeling. *Int. J. Numer. Anal. Methods Geomech.* **2024**, *48*, 2971–2995. [CrossRef]
29. Yan, N.; Hao, Z.M.; Bai, X.Y.; Cui, L.; Yin, J.C.; Liu, C.; Zhang, Y.M. Load-bearing characteristics and optimization design for rock-socketed bored piles in sandy silty clay in coastal areas. *Soil Dyn. Earthq. Eng.* **2025**, *190*, 109207. [CrossRef]
30. Gutiérrez-Ch, J.G.; Melentijevic, S.; Senent, S.; Jimenez, R. DEM modelling of shaft load transfer behavior of rock-socketed piles. *Comput. Geotech.* **2025**, *181*, 107149. [CrossRef]
31. Xu, J.J.; Cui, Z.H.; Qian, K.; Sun, X.; Xu, J. Three-Dimensional Numerical Analysis and Engineering Evaluation of Stilling Basin and Foundation Bedrock of Kala Hydropower Station, China. *Front. Phys.* **2022**, *9*, 807506. [CrossRef]
32. Li, W.; Wu, W.W.; Zhang, J.C. Numerical Stability Analysis of the Dam Foundation Under Complex Geological Conditions at Great Depth: A Case Study of Kala Hydropower Station, China. *Front. Phys.* **2022**, *9*, 808840. [CrossRef]
33. Liu, S.Q.; Wang, H.L.; Cheng, Z.C.; Li, W.; Ji, F. The formation process and stability analysis of dam site slope in Kala hydropower station through discrete element method. *Bull. Eng. Geol. Environ.* **2025**, *84*, 570. [CrossRef]
34. Roh, Y.; Kim, G.; Kim, I.; Kim, J.; Jeong, S.; Lee, J. Lessons Learned from Field Monitoring of Instrumented Piled-Raft Bearing in Rock Layer. *J. Geotech. Geoenvironmental Eng.* **2019**, *145*, 05019005. [CrossRef]

35. Asem, P.; Gardoni, P. On the Use and Interpretation of In Situ Load Tests in Weak Rock Masses. *Rock Mech. Rock Eng.* **2021**, *54*, 3663–3700. [CrossRef]
36. Chung, J.H.; Ko, J.; Klammler, H.; McVay, M.C.; Lai, P. A numerical and experimental study of bearing stiffness of drilled shafts socketed in heterogeneous rock. *Comput. Struct.* **2012**, *90–91*, 145–152. [CrossRef]
37. Johari, A.; Talebi, A. Stochastic Analysis of Piled-Raft Foundations Using the Random Finite-Element Method. *Int. J. Geomech.* **2021**, *21*, 04021020. [CrossRef]
38. Dong, X.L.; Tan, X.H.; Lu, Z.T.; Zhang, P.F.; Zha, F.S.; Xu, L. Reliability analysis of two-pile group in spatially variable soil considering differential settlement. *Ocean Eng.* **2024**, *307*, 118182. [CrossRef]
39. Kim, K.N.; Lee, S.H.; Kim, K.S.; Chung, C.K.; Kim, M.M.; Lee, S. Optimal pile arrangement for minimizing differential settlements in piled raft foundations. *Comput. Geotech.* **2001**, *28*, 235–253. [CrossRef]
40. Nguyen, D.D.C.; Kim, D.S.; Jo, S.B. Settlement of Piled Rafts with Different Pile Arrangement Schemes via Centrifuge Tests. *J. Geotech. Geoenvironmental Eng.* **2013**, *139*, 1690–1698. [CrossRef]
41. Nguyen, D.D.C.; Kim, D.S.; Jo, S.B. Parametric study for optimal design of large piled raft foundations on sand. *Comput. Geotech.* **2014**, *55*, 14–26. [CrossRef]
42. Reul, O.; Randolph, M.F. Design strategies for piled rafts subjected to nonuniform vertical loading. *J. Geotech. Geoenvironmental Eng.* **2004**, *130*, 1–13. [CrossRef]
43. Cho, J.; Lee, J.H.; Jeong, S.; Lee, J. The settlement behavior of piled raft in clay soils. *Ocean Eng.* **2012**, *53*, 153–163. [CrossRef]
44. Eid, H.T.; Shehada, A.A. Estimating the Elastic Settlement of Piled Foundations on Rock. *Int. J. Geomech.* **2015**, *15*, 04014059. [CrossRef]
45. Horikoshi, K.; Randolph, M.F. A contribution to optimum design of piled rafts. *Geotechnique* **1998**, *48*, 301–317. [CrossRef]
46. Bagheri, M.; Ranjbar Malidarreh, N.; Ghaseminejad, V.; Asgari, A. Seismic resilience assessment of RC superstructures on long–short combined piled raft foundations: 3D SSI modeling with pounding effects. *Structures* **2025**, *81*, 110176. [CrossRef]
47. Daraei, A.; Sherwani, A.F.H.; Faraj, R.H.; Kalhor, Q.; Zare, S.; Mahmoodzadeh, A. Optimization of the outlet portal of Heybat Sultan twin tunnels based on the value engineering methodology. *SN Appl. Sci.* **2019**, *1*, 270. [CrossRef]
48. Daraei, A.; Zare, S. A new strain-based criterion for evaluating tunnel stability. *Geomech. Eng.* **2018**, *16*, 205–215. [CrossRef]


**Disclaimer/Publisher's Note:** The statements, opinions and data contained in all publications are solely those of the individual author(s) and contributor(s) and not of MDPI and/or the editor(s). MDPI and/or the editor(s) disclaim responsibility for any injury to people or property resulting from any ideas, methods, instructions or products referred to in the content.